An Anthracene-Based Metal-Organic Framework for Selective Photo-Reduction of Carbon Dioxide to Formic Acid Coupled with Water Oxidation

Mostakim SK[+],[a] Soumitra Barman[+],[b] Shounik Paul,[b] Ratnadip De,[b] S. S. Sreejith,[b] Helge Reinsch,[c] Maciej Grzywa,[d] Norbert Stock,[c] Dirk Volkmer,[d] Shyam Biswas,*[a] and Soumyajit Roy*[b]

Abstract: A Zr-based metal-organic framework has been synthesized and employed as a catalyst for photochemical carbon dioxide reduction coupled with water oxidation. The catalyst shows significant carbon dioxide reduction property with concomitant water oxidation. The catalyst has broad visible light as well as UV light absorption property, which is further confirmed from electronic absorption spectroscopy. Formic acid was the only reduced product from carbon dioxide with a turn-over frequency (TOF) of 0.69 h^{-1} in addition to oxygen, which was produced with a TOF of 0.54 h^{-1}. No external photosensitizer is used and the ligand itself acts as the light harvester. The efficient and selective photochemical carbon dioxide reduction to formic acid with concomitant water oxidation using Zr-based MOF as catalyst is thus demonstrated here.

Introduction

In recent times, the capture and conversion of carbon dioxide (CO_2) to various value-added chemical feedstocks is of immense importance due to rising issues of global warming and excessive fossil fuel depletion. In this context, the development of efficient photocatalysts for CO_2 reduction to chemical feedstocks like HCOOH is one of the promising solutions. When this reductive process is coupled with a water oxidation reaction, the catalysis becomes much greener and more sustainable. Herein, we have achieved this goal using a Zr-MOF based catalyst which possesses light-harvesting property, generation of long-lived photo-induced excited states with effective charge migration to the catalytic centre. Thus, CO_2 reduction reaction by Zr-MOF was conducted in the UV/Vis region, where it showed efficient and selective reduction of CO_2 to HCOOH with a maximum turnover frequency (TOF) of 0.69 h^{-1}. On the other hand, O_2 was produced by water oxidation reaction with effective TOF of 0.54 h^{-1}.

In the past decades, several photocatalysts such as TiO_2,[1] $BiVO_4$,[2] $BiWO_6$,[3] $ZnGa_2O_4$,[4] Zn_2GeO_4,[5,6] metal-incorporating mesoporous silica such as ZrCu(I)-MCM-41, Cu_2O-loaded Zn-Cr layered double hydroxides[7,8] soft-oxometalates[9,10] and coordination polymers[11] have been widely explored as a potential candidates for photochemical CO_2 reduction. MOFs are a class of crystalline porous organic-inorganic hybrid materials with extended 3D network having high porosity and considerable interactions with the CO_2 molecule thus finding potential applications in gas separation,[12,13] gas storage[14,15] and especially CO_2 capture.[16–18] Besides, the metal clusters present in the MOFs are redox active whereas the organic linkers facilitate the electron transfer process. Moreover, these organic linker antennae can absorb light to photo-excite the metal cluster, which serves as redox photosensitizer and separates the electron-hole pair to facilitate redox processes.

In the past few years, the versatile activities of MOFs in water oxidation[19–21] and CO_2 photo-reduction[22–36] reactions have been explored. A porphyrin-based semiconducting Zr-MOF (PCN-222) was used as a catalyst for photo-reduction of CO_2 by Zhang et al.[26] The photochemical CO_2 reduction with amine-functionalised Ti and Zr-based MOFs was reported by Li

[a] *Dr. M. SK,[+] Dr. S. Biswas*
Department of Chemistry
Indian Institute of Technology
Guwahati, Assam, 781039 (India)
E-mail: sbiswas@iitg.ernet.in

[b] *Dr. S. Barman,[+] S. Paul, R. De, Dr. S. S. Sreejith, Prof. Dr. S. Roy*
Eco-Friendly Applied Materials Laboratory
Department of Chemical Sciences
New Campus, IISER-Kolkata
Mohanpur, West Bengal, 741246 (India)
E-mail: s.roy@iiserkol.ac.in

[c] *Dr. H. Reinsch, Dr. N. Stock*
Institut für Anorganische Chemie
Christian-Albrechts-Universität
Max-Eyth-Strasse 2, 24118 Kiel (Germany)

[d] *Dr. M. Grzywa, Prof. Dr. D. Volkmer*
Institute of Physics, Chair of Solid State Science
Augsburg University
Universitätsstrasse 1, 86135 Augsburg (Germany)

[+] *These authors contributed equally to this work.*

Supporting information and the ORCID identification number(s) for the author(s) of this article can be found under:
https://doi.org/10.1002/chem.202004596.

et al.[37–39] in acetonitrile solvent with triethanolamine (TEOA) as sacrificial agent. Very recently, the CO_2 photo-reduction to formate was reported by an anthracene-based MOF where the optically active anthracene chromophore acts as the antenna to transfer electrons into the Zr–O cluster.[40] On the other hand photochemical water oxidations by MOFs are well known. For instance, a visible light ($\lambda > 420$ nm) driven photocatalytic water oxidation has been reported using Fe-based MOFs to produce oxygen with $AgNO_3$ as the sacrificial electron acceptor.[41] On the other hand, cobalt-POMs $[(PW_9O_{34})_2Co_4(H_2O)_2]_{10}^-$ when immobilized in the hexagonal channels of a Zr^{IV} porphyrinic metal-organic framework exhibit high catalytic activity towards water oxidation.[42] However, very few reports exist for the photochemical CO_2 reduction coupled with water oxidation process. Frei and co-workers used heteronuclear bimetallic systems extensively to perform CO_2 reduction coupled water oxidation.[7] Various donor (Co, Mn)–acceptor (Ti, Zr) systems bridged by oxygen atoms were investigated.[43,44] Recently, we have shown photochemical CO_2 reduction coupled with water oxidation with Mn-based polyoxometalate (POM), Mo-based softoxometalate (SOM) and Cu–W-based SOM.[9,10] Taking into account the above mentioned possibilities of both CO_2 reduction and water oxidation using MOF based systems, we herein synthesized and characterized an anthracene-based Zr-MOF (**1**), the activated form (**1**′) of which the latter is an efficient photocatalyst for the CO_2 reduction and water oxidation. The CO_2 reduction reaction was conducted in the UV/Vis region, where it showed efficient and selective reduction of CO_2 to formic acid coupled with water oxidation reaction.

Results and Discussion

Structural analysis

The crystal structure of **1** was calculated by using the structure of PIZOF-2 as the starting model.[45] The details of the calculation process have been provided in the "Rietveld refinement" sub-section under Experimental Section. A remarkable similarity was observed between the experimental and calculated XRPD patterns of **1** (Figure S1, Supporting Information). The as-synthesized compound contains guest DMF and water molecules in the pores. It must be activated (i.e., become guest-free) before the catalytic application. The substrate molecules can diffuse into the pores of the activated compound during photo-catalysis and interact with the active sites of the framework. Hence, the as-synthesized **1** (100 mg) was stirred in methanol (30 mL) for overnight. Then, the methanol-exchanged material was heated under high vacuum at 120 °C for 8 h to get the activated form of the material (denoted as **1**′). The refined cell parameters and space group of activated **1**′ ($Fd\bar{3}$, $a = 39.224(3)$ Å) show considerable agreement with those of PIZOF-2 ($Fd\bar{3}m$, $a = 39.8144(11)$ Å). A Rietveld refinement was attempted. The Rietveld plots presented in Figure S2 (Supporting Information) exhibit very good agreement between the experimental XRPD pattern and the XRPD pattern calculated based on the crystal structure of **1**.

The morphology of the particles of activated **1**′ was analysed by FE-SEM and HR-TEM measurements. The FE-SEM and HR-TEM images show that the compound crystallized as homogeneously formed octahedral crystals (Figures S3&S4, Supporting Information). These results are consistent with the cubic crystal structure of the Zr-MOF, as confirmed by the XRPD experiments.

The crystal structure of **1** is quite similar with NNU-28 and PIZOF series of Zr-MOFs.[40,45] The ligand of **1** contains ethylene groups, instead of ethynylene units in NNU-28 and PIZOF-2. In addition, both **1** and NNU-28 have anthracene units between the ethylene/ethynylene groups. The chemical structures of these ligands are exhibited in Scheme 1. The framework of **1** is

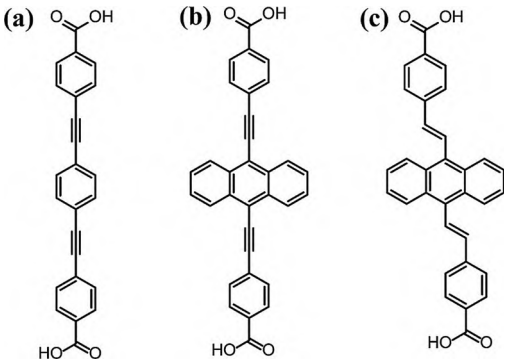

Scheme 1. Structures of the ligands used for the synthesis of (a) PIZOF-2, (b) NNU-28 and (c) compound **1**.

briefly described here, since the structures of the isotypic Zr-MOFs have been already reported. The presented compound possesses a two-fold interpenetrated framework structure (Figure 1). Each framework is composed of $[Zr_6O_4(OH)_4(\mathbf{L})_6]^{12+}$ clusters as the inorganic building units, which are inter-linked with each other by the carboxylate groups of twelve $H_2\mathbf{L}$ ligands. All the Zr^{4+} ions have square-antiprismatic geometry. Every independent framework contains eight tetrahedral and four octahedral cavities. The interpenetration of the two distinct networks causes reduction of the "octahedral" cavities into tetrahedral cavities. Thus, the interpenetrated structure bears concave and convex tetrahedral cavities, which have free diameters of ≈13 and ≈19 Å, respectively.

FTIR spectroscopy, thermal and chemical stability

The FTIR spectra of the as-synthesized and activated **1** are shown in Figure S6 in the Supporting Information. In both the spectra, the asymmetric and symmetric stretching vibrations of the coordinated $H_2\mathbf{L}$ ligand give rise to bands at 1600 and 1414 cm^{-1}, respectively.[46,47]

The thermal stability of the Zr-MOF was evaluated by thermogravimetric (TG) experiments. The results show that the material is stable up to 270 °C (Figure S8, Supporting Information). The TG trace of as-synthesized **1** shows two weight loss steps below 270 °C. In the temperature range 25–120 °C, the weight loss of 5.1% is associated with the removal of twelve water

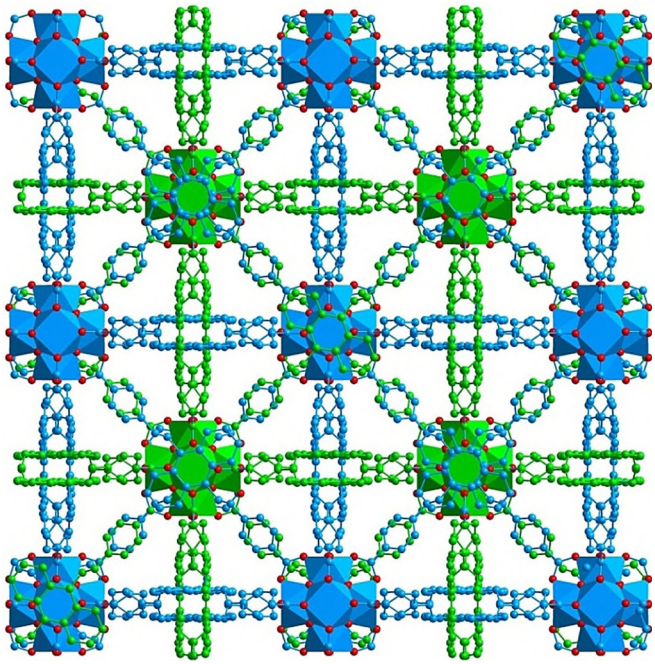

Figure 1. Structure of **1** showing its two-fold interpenetrated framework. The two independent frameworks are shown in blue and green. The O atoms are displayed in red.

molecules per formula unit (calcd: 5.2%). From 120 to 200 °C, a weight loss of 10.9% is observed, which can be related to the elimination of six DMF molecules per formula unit (calcd: 10.6%). From the TG curve of **1′**, the number of missing ligands per Zr_6 unit has been found to be 1.09 (Figure S9, Supporting Information).[48]

The chemical stability of the Zr-MOF was checked in water as well as in NaOH and HCl solutions in the pH range of 1–12 at room temperature for 24 h. For this purpose, the XRPD patterns of the compound were recorded after stirring in these liquids. The MOF samples recovered by filtration after the stirring, showed complete retention of crystallinity (Figures S10&S11, Supporting Information), suggesting high chemical stability of the framework structure.

Gas sorption characteristics

Nitrogen sorption experiment was carried out to determine the BET surface area of activated **1′**. The BET surface area, which was calculated from the adsorption isotherm (Figure S12, Supporting Information) in the p/p_0 range of 0.03–0.10, was found to be 997 $m^2 g^{-1}$. The micropore volume was estimated as 0.55 $cm^3 g^{-1}$ at p/p_0 value of 0.51. The pore size distribution plot (Figure S13, Supporting Information) revealed the presence of a maximum at 6.4 Å of half pore width, which equals to the pore diameter of 12.8 Å. Furthermore, CO_2 adsorption analysis was carried out with the activated Zr-MOF at 0 °C. The material showed a CO_2 adsorption capacity of 47 $cm^3 g^{-1}$ at 0 °C and 1 bar (Figure S14, Supporting Information). The good CO_2 adsorption capacity of **1′** could be attributed to the existence of open metal sites at the defect centers which allows strong interactions with CO_2.[49]

Photophysical properties

Material **1′** shows both UV and broadband visible light absorption in the range from 200 nm to 600 nm (Figure 2a), which makes it an efficient photocatalyst. This allows for promoting the electrons of **1′** to an excited state upon visible-light irradiation. Mott–Schottky plots were measured in three different frequencies (500, 1000, 1500 Hz) where the flat band potential

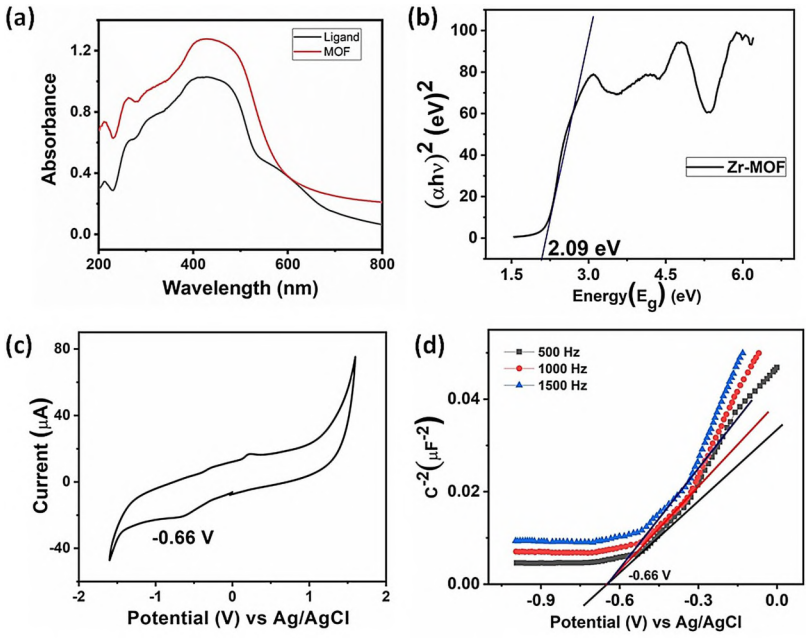

Figure 2. (a) Diffuse reflectance UV/Vis spectra of **1′** and H_2L. (b) Plot of $(\alpha h\nu)^2$ versus photon energy for **1′**(direct allowed electronic transition) where we assume the crystal momentum of electrons and holes are same in both valence and conduction band. (c) Cyclic voltammogram of **1′** in water with scan rate 100 mV s^{-1}. (d) Mott–Schottky plots for **1′** in 0.5 M Na_2SO_4 aqueous solution (pH 6.6).

lies at ≈−0.66 V vs. Ag/AgCl (−0.46 V vs. NHE). The positive slope of the linear plot indicates the n-type nature for the semiconductor catalyst and the flat band potential is considered to be the bottom of the conduction band (LUMO)[50,51] (Figure 2d). Further electrochemical study of **1′** (from cyclic voltammogram, Figure 2c) reveals the onset reduction potential at −0.66 V versus Ag/AgCl (i.e., −0.46 V versus NHE), supporting the flat band potential. From the TAUC plot (Figure 2b) the band gap energy of **1′** is calculated to be 2.09 eV and the valence band (HOMO) is then measured as 1.63 V versus NHE.

Thus, it is theoretically possible to photochemically reduce CO_2 to formate over the Zr-MOF as its LUMO lies below the reduction potential of CO_2 to formate (−0.28 V versus NHE).[26] On the other hand, water can be easily oxidized to O_2, as the redox value for water oxidation is 0.81 V (versus NHE at pH 7), which lies in between the HOMO and LUMO.

Photochemical CO_2 reduction in water

Photocatalytic reduction of CO_2 was conducted with **1′** (due to its high CO_2 capturing ability) under both UV and visible light irradiation. Remarkably, **1′** exhibited significant photocatalytic activity for CO_2 reduction and formic acid (HCOOH) is obtained as the only reduced product, which was quantified by GC-MS and high-performance liquid chromatography (HPLC). Further cyclic voltammetric experiments were carried out where we found a considerable shift and an increase in current density in the redox couple which ensures the formation of new species and the corresponding redox process is getting favoured under CO_2 atmosphere (Figure 3a). A time-dependent study showed a continuous increase of formate ($HCOO^-$) over time and a maximum 26 μmol of formate was produced in 16 h under the ambient conditions (Figure 3b). No other reduced gaseous or liquid product could be detected by GC-MS, which suggests high selectivity towards CO_2 reduction products. Subsequently, water was oxidized to form O_2 and the time-dependent measurement was carried out (Figure 3d) by GC-MS and YSI (Yellow Springs Instrument) dissolve oxygen meter (Clarke electrode). It is notable that 9 μmol of O_2 was produced in a reaction time of 16 h. The theoretical value of CO_2 reduced product and O_2 production should be 2:1 for the coupled reaction. However, it is difficult to match the exact ratio with the theoretical value. But, in our reaction the yield of oxygen is low, which may be because of the partial loss due the measurement in Clarke electrode. Same experiment was repeated with only ligand (H_2**L**) where a mixture of reduced products (HCHO and HCOOH) was obtained only when the sacrificial electron donor (TEOA) was used. As shown in Figure 3b the initial concentration of HCOOH was high as compared to the produced HCHO however as the reaction proceed the concentration of HCOOH in the reaction mixture diminishes with marked increase in the concentration of HCHO showing the possibility of HCOOH as a potential intermediate for the catalytic conversion of CO_2 to HCHO. Also, the yields of the CO_2 reduced products are less in comparison with that of **1′**. After 16 h of reaction time, ≈11 μmol of HCHO and ≈4 μmol of HCOOH was obtained (Figure 3b). The ligand did not participate in water oxidation reaction, which is evident from the CV taken during the photocatalysis, in which there is no current rise in the anodic region (Figure S15, Supporting Information). The selective formation of HCOOH using **1′** may be due to the fact that the LUMO level is closer to the potential of HCOOH

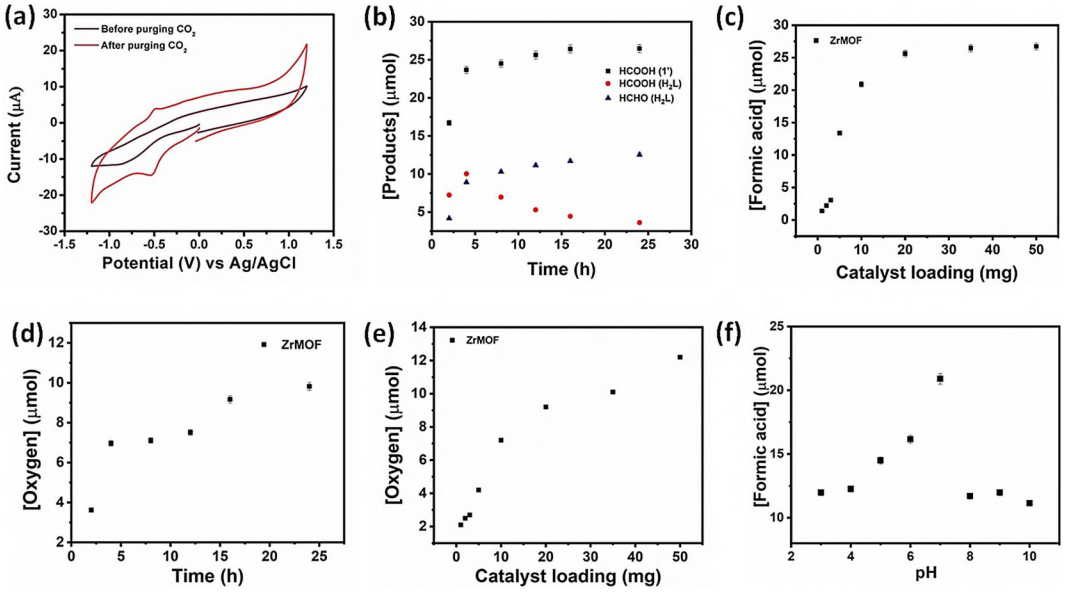

Figure 3. (a) Cyclic voltammogram (CV) of CO_2 reduction reaction. The black line represents the CV plot before purging CO_2 whereas the red line denotes the CV plot after purging CO_2 which shows considerable change in current density. (b) Time-dependent plot of products formation using **1′**. (c) Plot of amount of formic acid produced with different catalyst (**1′**) loadings. (d) Time-dependent study of O_2 production using **1′**. (e) Plot of amount of O_2 evolved with different catalyst (**1′**) concentrations. (f) pH-dependent study of formic acid production using **1′. N.B**: The reaction was carried out in a quartz cuvette and kept in the photoreactor under UV-light (150 W lamp, λ = 280–400 nm, illuminance 19 mW cm^{-2}). To perform controlled experiments, 20 mg of Zr-MOF and ligand were taken in each case.

formation and also owing to the presence of Zr^{4+}/Zr^{3+} couple. The multi-redox Zr couple acts synergistically with the ligand framework to assist the selective reduction of CO_2 to HCOOH.

In the case of **1′**, a detailed pH-dependent study was performed. Both CO_2 reduction and water oxidation are proton-dependent processes, so the overall reaction equilibrium depends on the concentration of proton in the reaction medium. Therefore, the pH of the reaction medium was varied within the stability window of the catalyst to optimize the reaction conditions and the maximum yield was found at pH 7 (Figure 3 f). This result is in accordance with CV result where we got maximum current for the solution at pH 7 (Figure S16, Supporting Information). This fact was observed mainly because of the two proton-coupled opposite processes. Due to the water oxidation process, the electrons released in the reaction medium are transferred to the reaction sites, which are further taken up for the CO_2 reduction [Eqs. (1) and (2)]. These facts imply that the maximum yield would occur at the intermediate pH value. Then, the catalyst loading was varied up to 50 mg at pH 7. The amount of formate increased gradually with increasing catalyst loading up to 50 mg and after that the product formation became saturated with increasing catalyst loading (Figure 3 c and 3 e and Figure S17, Supporting Information). This is may be due to limited solubility of CO_2 in water. However, the observed aspect can be explained from the reaction kinetics point of view. As, this reaction follows first order kinetics (Figure 4 a and 4 d), it is logical to say that the product formation gets saturated after certain point of time depending on the condition.

$$2\,H_2O \rightarrow O_2 + 4\,H^+ + 4\,e^- \quad (1)$$

$$CO_2 + 2\,H^+ + 2\,e^- \rightarrow HCOOH \quad (2)$$

No formic acid was detected when the reaction was carried out in the dark, which implies that the reaction is a light-driven process. After performing the reaction under light, the product was detected in ^1H NMR where a characteristic peak for $HCOO^-$ is found at 8.1 ppm (Figure 4 a). Further, to confirm the origin of $HCOO^-$, isotopic $^{13}CO_2$ was used in the photocatalytic reaction condition and the product was characterized by ^{13}C NMR spectroscopy. We found the characteristic peak for $H\text{-}^{13}COO^-$ at 165 ppm (Figure 4 c). This fact confirms that the carbon present in the formate moiety is generated from carbon dioxide. Also, a doublet ($^1J_{CH} = 214$ Hz) is observed at 8.1 ppm in ^1H NMR where the proton is coupled with ^{13}C atom (Figure 4 b). From ^{13}C NMR (without proton decoupling) measurement, the same coupling constant ($^1J_{CH} = 214$ Hz) is also obtained (Figure 4 d). Besides, a deuterium-labelling experiment was conducted using D_2O as a solvent instead of H_2O. We found that the deuterium was incorporated into the formate moiety, which was confirmed from mass spectrometry (Figure S18, Supporting Information). As we get exchangeable D in the reaction medium, it got incorporated during the formation of formic acid and later we have obtained deuterium incorporated ethyl formate after reaction with ethanol. Subsequently, isotopic H_2O^{18} and H_2O^{16} were used for finding the source of oxygen in the reaction medium. We found oxygen in the mass spectrum where all the oxygen species that is, $O^{16}O^{16}$, $O^{16}O^{18}$ and $O^{18}O^{18}$ were present in the reaction medium (Figure S19, Supporting Information). This result concludes that the oxygen was produced by water oxidation reaction.

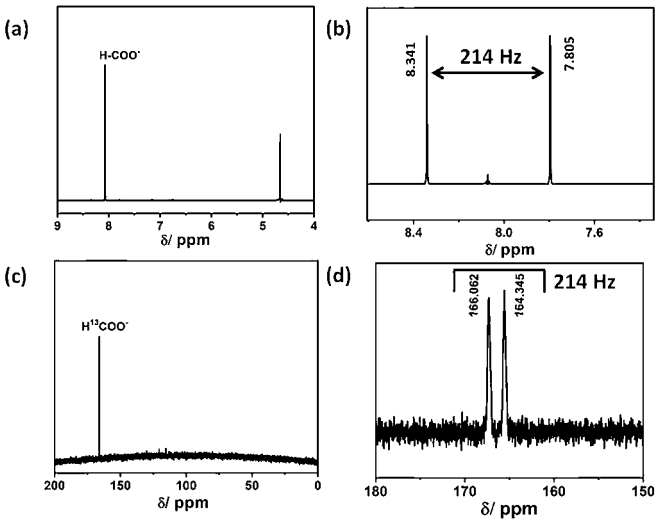

Figure 4. (a) ^1H NMR spectrum of formic acid after solvent (H_2O) suppression method. (b) ^1H NMR spectrum after 16 h of irradiation using $^{13}CO_2$ (c) ^{13}C NMR spectrum of the reaction mixture with $^{13}CO_2$. (d) ^{13}C NMR spectrum without proton decoupling after 16 h of irradiation.

Photocatalytic CO_2 reduction by Zr-MOFs has been documented in several reports in which maximum yield of formic acid obtained was 183.3 μmol (Table 1). Here, we have obtained maximum 345.6 $\mu mol/mmol_{MOF}$ of formic acid with concomitant water oxidation, which is significantly higher than all the Zr-MOF catalysts reported for CO_2 photo-reduction (Table 1). In this study, we have not used any sacrificial electron donor like TEOA, and water itself acts as an electron donor to produce O_2. Thus, it is a coupled process of water oxidation with CO_2 reduction, giving valorised CO_2 to formate and environmentally benign oxygen as products.

Wavelength-dependent studies were performed to ensure the role of induced light on the production of formic acid (Figure S20, Supporting Information). The reaction was carried out under different wavelengths under same reaction condition. The production rate of the product matches well with the photon absorption capability of the Zr-MOF. It also confirms that the reaction rate is induced with the incident radiation.

The catalyst could be reused up to 10 catalytic cycles and the yield was almost same for those cycles (Figure S21, Supporting Information). We have observed a decrease of 4 μmol of formic acid after ten cycles, which might be due to loss after repeated filtration and re-suspension cycles of the catalyst from the reaction medium.

Stability of the catalyst

The stability of the catalyst **1′** during the photocatalytic reaction was confirmed by electronic absorption and FTIR spectroscopy. In the FTIR spectra of **1′**, the two bands at 1600 and 1414 cm^{-1} are associated to the in- and out-of-phase stretch-

Table 1. Photochemical CO_2 reduction to formic acid by Zr-based MOFs.

Catalyst	TOF [$\mu mol\, h^{-1}\, mmol_{MOF}^{-1}$]	Catalytic Sites	Composition	Electron donor	Ref.
H_2N-UiO-66(Zr)	46.3	metal centre	$Zr_6O_4(OH)_4(L^1)_6$	triethanolamine (TOEA)	[39]
Mixed H_2N-UiO-66(Zr)	73.4	metal centre	$Zr_6O_4(OH)_4(L^1)_{4.8}(L^2)_{1.2}$	TOEA	[39]
H_2N-UiO-66(Zr,Ti)-120—116	71.9	metal centre	$Zr_{2.6}Ti_{3.4}O_4(OH)_4(L^1)_6$	TOEA	[38]
Zr-SDCA-NH	96.2	metal centre, ligand	$[Zr_6O_4(OH)_4(L^4)_6]$	TOEA	[52]
PCN-222	143.5	metal centre	$Zr_6(\mu_3\text{-}OH)_8(OH)_8(TCPP)_2$	TOEA	[26]
NNU-28	183.3	metal centre, ligand	$Zr_6O_4(OH)_4(L^3)_6$	TOEA	[40]
1′	345.6	metal centre, ligand	$Zr_6O_4(OH)_4(L)_6$	water	this work

$H_2\mathbf{L}^1$ = 2-Aminoterephthalic acid, $H_2\mathbf{L}^2$ = 2,5-diaminoterephthalic acid, $H_2\mathbf{L}^3$ = 4,4′-(anthracene-9,10-diylbis(ethyne-2,1-diyl))dibenzoic acid, $H_2\mathbf{L}$ = 4,4′-(anthracene-9,10-diylbis(ethane-2,1-diyl))dibenzoic acid and H_4TCPP = tetrakis(4-carboxyphenyl)-porphyrin.

ing of carboxylate group present in the ligand molecule (Figure S6, Supporting Information). The modes due to OH and CH bending are mixed with the Zr–O modes (847, 759, 627 and 482 cm^{-1}) at lower frequencies. The catalyst showed similar FTIR spectra before and after photocatalytic reaction (Figure 5 A).

Similarly, the electronic absorption spectra of **1**′ retained all the absorption peaks before and after photocatalytic CO_2 reduction, which verified the stability of the catalyst (Figure 5 B).

Scanning electron microscopy (SEM) images were recorded for the Zr-MOF photocatalyst in water dispersion before and after the reaction. The morphology was similar in both the cases, which depicts that the catalyst can be reused for several cycles (Figure 5 C).

X-ray powder diffraction (XRPD) experiments were carried out for the Zr-MOF before and after photocatalytic experiments, in which it showed significant stability. All the Bragg peaks after one cycle of photocatalysis were similar with the activated materials **1**′. There was some decrease in intensity of the peaks after five cycles of photocatalysis, although the Bragg peak positions were similar with **1**′. However, after ten cycles of photocatalysis, **1**′ significantly lost its crystallinity and the positions of Bragg peaks did not match with **1**′. These XRPD results (Figure S10, Supporting Information) suggested that the activated material **1**′ can be reused in the photocatalysis reaction for more than one cycle. N_2 sorption isotherms at −196 °C were collected with material **1**′ after one and ten cycles of photocatalysis. The BET surface areas of this material after one, five and tenth cycles were found to be 745, 138 and 9 $m^2\, g^{-1}$, respectively (Figures S22&S23, Supporting Information). Thus, the material remained porous after the one photocatalytic experiment with slight reduction in porosity as compared to the material before the photo-catalytic experiment (Figure S12, Supporting Information). After ten cycles of photocatalysis, the material became non-porous.

Mechanistic pathway for the reaction

A plausible mechanism of the photocatalytic reduction pathway is illustrated in Scheme 2. Periodic DFT calculations of the

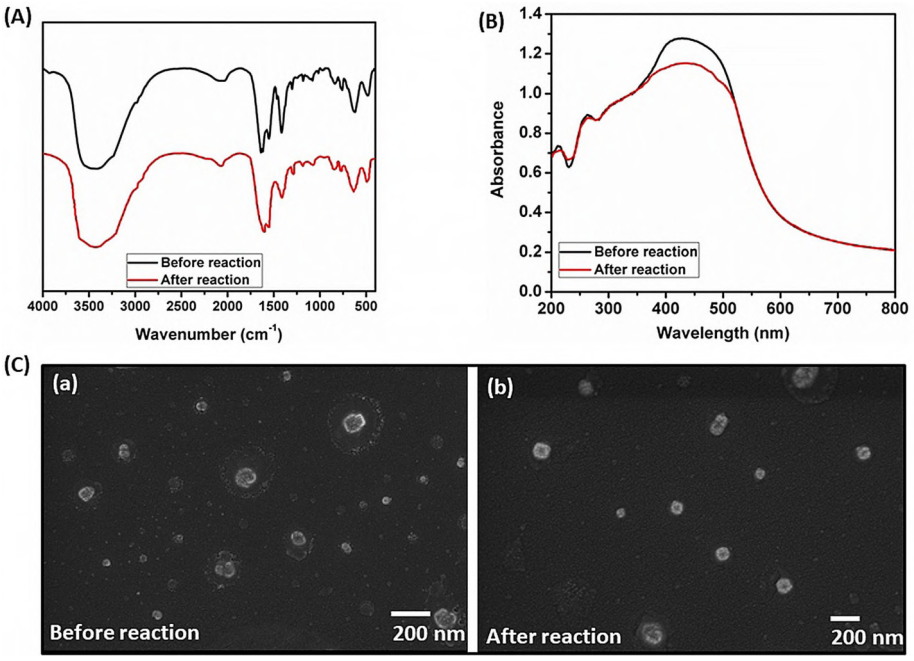

Figure 5. (A) FTIR spectra of **1**′ before and after photochemical CO_2 reduction. (B) Electronic absorption spectra of **1**′ before and after reaction. (C) SEM images of the aqueous dispersion of **1**′ before (a) and after (b) reaction.

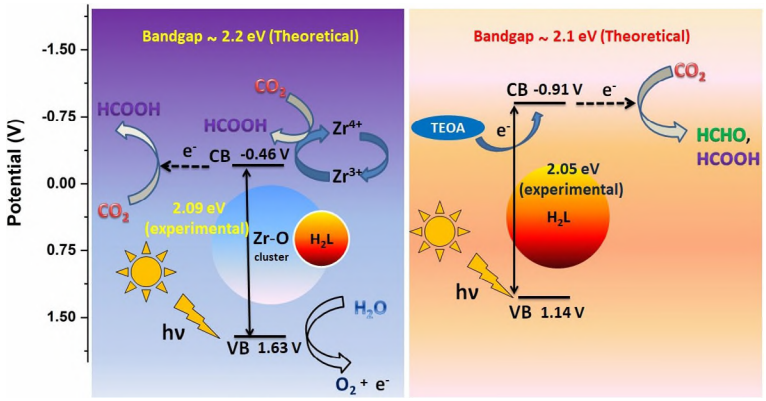

Scheme 2. Illustration of the photocatalytic route for CO_2 reduction using **1**′ and H_2**L**.

HOMO–LUMO gap (cluster calculation) or the band gap (periodic calculation) show that the frontier orbitals are exclusively dominated by the π–π* transitions of the organic ligand (Figure S24, Supporting Information). This fact can also be attributed to the similar band gap for both **1**′ and H_2**L** ligand from TAUC plot considering direct allowed transition. When ligand (H_2**L**) is photo irradiated (Scheme S2, Supporting Information), it harvests light and gets photo-excited. The light-absorbing property of the ligand is evident from the diffuse reflectance spectra and EPR measurement where there was an enhancement of the peak at ≈336.5 mT with a corresponding *g*-value of 2.005 (Figure S25, Supporting Information). The free electrons present in the system (from TEOA donor) then reduce carbon dioxide to HCHO and HCOOH. On performing time dependent study, it is found that the amount of HCOOH dominated over the yield of HCHO during the initial period of time. As time progresses, the yield of HCOOH decreased with a concomitant increase in HCHO concentration (Figure 3 b). The production of HCHO with ligand may be due to the position of LUMO level at a more negative value (−0.91 V vs. NHE) as compared to that of **1**′ (−0.46 V vs. NHE). As opposed to **1**′, water oxidation was not observed in the case of ligand possibly due to the fact that the energy of HOMO level of the ligand is less when compared to **1**′ which limits its ability to oxidize water. Moreover, in a stepwise water oxidation mechanism (shown in Supporting Information), it usually requires two water (or hydroxide) ligand coordinated with a single or two adjacent metal sites. Upon oxidation of these water (or hydroxide) ligands, the O–O bond could be formed in a controlled fashion. Mechanistically, this seems only likely to occur at a metal center, but not for the case of a neat organic ligand. In the latter case the oxygen evolution reaction (OER) would have to follow radical pathways and presumably the formation of a putative OH* radical via $H_2O \rightarrow OH^* + e^{(-)} + H^{(+)}$ which is energetically so unfavorable that it cannot occur in solution with the photonic energy supplied. In addition, the freely diffusing OH* radicals would quickly lead to oxidation of the organic ligand.

On the contrary, when the experiment was repeated using Zr-based catalyst **1**′, HCOOH is obtained as the only reduced product apart from oxygen, which is generated via oxidation of water. The underlying mechanism can be explained as follows: The reaction is initiated with the photoexcitation of the chromophoric anthracene moiety in **1**′. Out of the photogenerated electron–hole pairs, the hole oxidises water to produce oxygen and electrons. Unlike the free ligand (H_2**L**), in **1**′ there is a possibility for the reduction of Zr^{4+} (d^0) to Zr^{3+} (d^1) using the generated electrons. This process can also contribute towards the oxidation of water to oxygen. The presence of Zr^{3+} during photo reduction was seen in EPR spectrum (Figure S26, Supporting Information) with a new peak at $g = 2.009$ corresponding to the intervalence change of the Zr–O cluster due to the LMCT process and the peak at $g = 2.003$ is due to the ligand. Later the Zr^{3+} species reduces CO_2 to HCOOH, getting itself oxidised to a Zr^{4+} species, completing the catalytic cycle. This reflects on the selectivity of **1**′ towards HCOOH production with respect to H_2**L** ligand where a mixture of products was observed (Scheme 2). Further, we have investigated the electron-transfer mechanism from Zr-oxo clusters of **1**′ to soluble CO_2 by XPS analysis (Figures S27–S29, Supporting Information). In the Zr 3d spectra (Figure S28, Supporting Information), the two peaks at 185.36 and 183.01 eV can be attributed to the presence of Zr^{4+} in the Zr-oxo clusters of **1**′ before photocatalysis. After photocatalysis of **1**′, the binding energies of the Zr-oxo clusters are slightly decreased (Figure S29, Supporting Information), which indicates that Zr^{4+} ions are in partially reduced form. We know that the binding energy is related with the valance charge of the ion. Therefore, the reduced binding energies of the Zr-oxo clusters can be ascribed to the presence of Zr^{3+} ions where the Zr^{3+} ion reduces CO_2 to formic acid during the photocatalysis. This result is consistent with the EPR analysis by which the formation Zr^{3+} ions during the photocatalysis of CO_2 to formic acid were confirmed.

Steady-state PL emission spectra for both Zr-MOF and Ligand shows significant PL emission quenching. This result leads to the fact that the electron-hole recombination in the whole photocatalytic process is considerably suppressed which results in the excellent photocatalytic ability of Zr-MOF and Ligand. The average lifetime of Zr-MOF and ligand are 1.9 ns and 1.4 ns, respectively. The presence of three sizable components in the excited state (44%, 25% and 29%) for Zr-MOF result in the accumulation of the photogenerated electrons

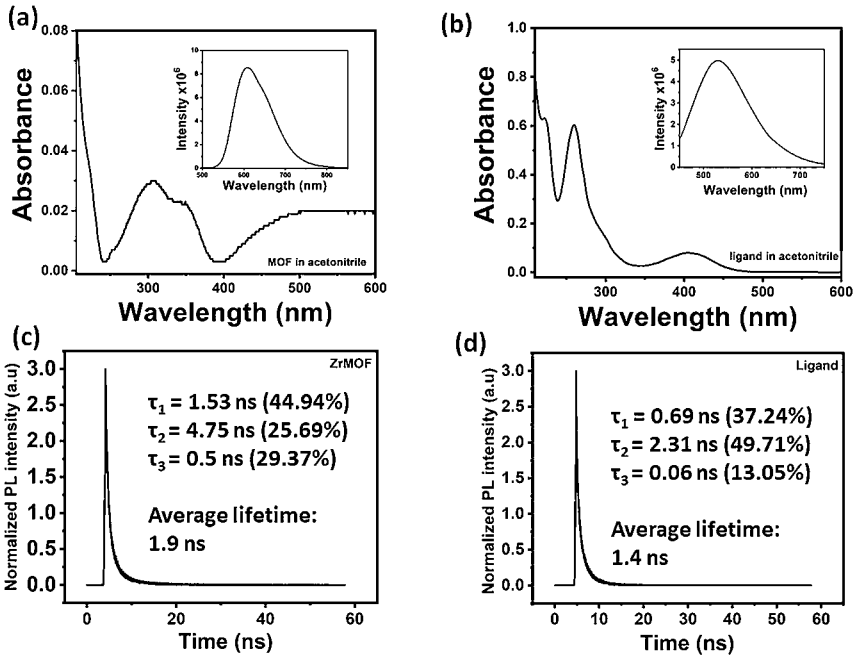

Figure 6. (a) Electronic absorption spectra of Zr-MOF in acetonitrile. In inset: PL emission of Zr-MOF under excitation at 350 nm (b) Electronic absorption spectra of H_2L in acetonitrile. In inset: PL emission of H_2L under excitation at 410 nm. (c) Time-resolved PL kinetics for Zr-MOF recorded with excitation at 350 nm and emission at 610 nm. (d) Time-resolved PL kinetics for H_2L recorded with excitation at 410 nm and emission at 530 nm.

which later get transferred to the active site leading to CO_2 reduction. Similarly, two components with distinct lifetimes (49%, 37%) dictate the transfer of electrons to the active site (Figure 6). Additionally, transient photocurrent response of Zr-MOF shows higher current density as compared to the H_2L depicting excellent charge separation of the charge carriers (Figure S39).

The main intrinsic factor in this whole catalytic process is the coupling of CO_2 reduction with water oxidation. Due to the water oxidation the generated electron accelerates the CO_2 reduction process which is believed to driven by water oxidation reaction. This can be explained form the results of CO_2 reduction where both ligand and Zr-MOF were employed as catalysts. In the case of ligand, the CO_2 reduction process proceeds only by the addition of external sacrificial electron donor (TEOA) which also limits its product yield since the coupling process is absent here. On contrary, in the case of Zr-MOF, the CO_2 reduction process is coupled with water oxidation. Owing to this coupling higher yield of CO_2 reduced product is obtained.

The main advantage using water as sacrificial electron donor is that it produces oxygen as the only by-product whereas the use of TEOA as a sacrificial electron donor, produces organic byproducts which may interfere with the reduction process.

Conclusions

We have reported both visible and UV light photo-reduction of CO_2 coupled with water oxidation by an anthracene-based Zr-MOF catalyst with high selectivity and significant production rate of 81.25 $\mu mol\,h^{-1}\,g^{-1}$ for CO_2 reduction of formic acid. The selective formation of formic acid of Zr-MOF over ligand may be due to the change in the frontier orbital energy. The good CO_2 adsorption capacity might allow the Zr-MOF to interact efficiently with CO_2 to produce formic acid in ambient reaction conditions without any sacrificial electron donor. The combined effect of the Zr-oxo cluster and the organic anthracene-based ligand enables the coupling of CO_2 reduction with water oxidation. The present study highlights mainly the incorporation of a light-harvesting anthracene moiety with Zr^{IV} ion, which shows photocatalytic behaviour towards CO_2 reduction-coupled water oxidation. The work could open up new avenues of water oxidation coupled with CO_2 reduction with porous framework materials.

Experimental Section

Materials and general methods

All reagents were received from commercial suppliers. Methyl 4-vinylbenzoate was synthesized according to the reported procedure.[53,54] The synthesis and characterization (Figure S31–S36) of the H_2**L** ligand are given in the Supporting Information.

Electronic absorption spectra (EAS) were recorded using a Jasco V-670 spectrophotometer. The spectra were collected for **1**′ and H_2**L** before performing photocatalysis. FTIR measurements were performed by the KBr pellet technique. Initially, a pellet was prepared from the mixture of KBr and the sample. FTIR spectra were recorded by using a PerkinElmer Spectrum RX1 or a PerkinElmer Spectrum Two spectrometer with FTIR facility in the range 4000–400 cm^{-1}. A Mettler-Toledo TGA/SDTA 851e thermogravimetric analyzer was used for performing the thermogravimetric analyses in the temperature range of 25–700 °C with a heating rate of 10 °C min^{-1} under air atmosphere. The X-ray powder diffraction (XRPD) patterns were collected with a Bruker D2 Phaser X-ray diffractometer working at 30 kV, 10 mA for using $Cu_{K\alpha}$ ($\lambda = 1.5406$ Å)

radiation. A Zeiss (Zemini) scanning electron microscope was utilized collecting the Field Emission—Scanning Electron Microscopy (FE-SEM) images. A JEOL, Model:2100F Field Emission Transmission Electron Microscope (FETEM) was utilized collecting the high-resolution images. The SEM images were recorded with a SUPRA 55 VP-41-32 Scanning Electron Microscope and analysed by using the Smart-SEM version 5.05 Zeiss software. The samples were prepared by drop casting very dilute dispersions onto silicon wafers and drying in dust free area. The argon sorption isotherms were measured by employing Quantachrome Autosorb iQ-MP and Quantachrome Autosorb 2QDS-30 gas sorption analyser at −196 °C. The CO_2 adsorption experiments were carried out with a Belsorp Max instrument combined with a BELCryo system at 0 °C. The samples were degassed under high vacuum at 120 °C for overnight before the gas sorption measurements. PAR model 273 potentiostat was used for the cyclic voltammetry (CV) experiment. A platinum wire auxiliary electrode, a glassy carbon working electrode with surface area of 0.0616 cm^2 and an aqueous Ag/Ag^+ reference electrode, which was filled with 0.1 M KCl solution, were used in a three-electrode configuration. All the measurements were performed at 25 °C in an inert atmosphere. The collection of the mass spectra was accomplished by using an Agilent 6520 Q-TOF high-resolution mass spectrometer (HR-MS). By employing a Bruker AM 600 spectrometer; the ^1H NMR spectra were measured for Ligand and catalyst characterization. The CO_2 reduced products were characterized by ^1H NMR and ^{13}C NMR. In ^1H NMR, solvent suppression method (water; presaturation method) was used and taken in 400 MHz Jeol NMR Spectrometer and coupling experiments were done in 500 MHz Bruker NMR Spectrometer.

Synthesis of $[Zr_6O_4(OH)_4(C_{32}H_{20}O_4)_6]\cdot 6DMF\cdot 12H_2O$ (1)

In a Pyrex tube, a mixture of $ZrOCl_2\cdot 8H_2O$ (17 mg, 0.053 mmol), H_2**L** ligand (25 mg, 0.053 mmol), acetic acid (181 μL, 1.58 mmol) and DMF (3 mL) was placed. The mixture was sonicated for 20 min at room temperature. Then, the mixture was heated at 70 °C for 120 h to give a yellow solid. The solid was filtered off, washed with copious amount of acetone and then heated in an oven at 70 °C for 5 h. Yield: 21 mg (0.0052 mmol, 59%) based on the Zr salt. IR (KBr): $\tilde{\nu}$ = 3643 (w), 3042 (w), 2200 (w), 1650 (w), 1596 (s), 1533 (m), 1409 (s), 1170 (m), 762 (m), 636 (s), 466 cm^{-1} (w).

Rietveld refinement

The XRPD pattern was measured in reflection geometry using $Cu_{K\alpha}$ radiation, and could be successfully indexed using TOPAS academics[55] with a cubic *F*-centered cell (a = 39.224(3) Å, extinction conditions suitable for space group $Fd\bar{3}$ (no. 203). The cell parameters and the space group symmetry thus agree well with the ones of PIZOF-2 (**F**$d\bar{3}m$, a = 39.8144(11) Å).[46] A suitable model was developed by converting the crystal structure of PIZOF-2 into a hypothetical structure exhibiting $Fd\bar{3}$ symmetry using Powdercell[56] in the sequence $Fd\bar{3}m \rightarrow Fd\bar{3}$. This transition is also necessary since the linker molecule in PIZOF-2 has a central mirror plane while the linker molecule discussed herein does not exhibit such symmetry. The hypothetical structure was further changed imposing the indexed cell parameters and converting the linker molecule to the employed one and subsequently optimized by force-field calculation using the universal force field as implemented in the Materials Studio software.[57] An attempted full Rietveld refinement of this model was not possible which we attribute to the conformational flexibility of the linker molecule, the large unit cell and also the low number of reflections above 20° (2θ). Nevertheless, refining only the position of the Zr-atoms and modelling residual solvent molecules by oxygen atoms inside the pores gives an excellent agreement with the experimental data. These guest atoms (G*n*) should be considered placeholders for any kind of solvent molecules. Some relevant parameters for the modelling are summarized in Table S2 (Supporting Information). The final Rietveld plots are shown in Figure S2 (Supporting Information).

General reaction procedure of photochemical reduction

Photocatalytic CO_2 reduction reactions were carried out as follows. Desired amount of catalyst (**1**′) is taken in a quartz shell containing 10 mL of degassed double-distilled water and sonicated for 6 h. Sonication is a very important step because it helps in attaining uniform dispersion of **1**′ in water solvent. The sonicated reaction mixture was sealed and CO_2 gas was purged for 2 h to saturate the solution. Then, the reaction mixture was taken in a Quartz cuvette and kept in the photoreactor under UV-light (150 W lamp, λ = 280–400 nm, illuminance- 19 mW cm^{-2}) and also repeated under Visible light (λ = 420–600 nm, illuminance-67 mW cm^{-2}) for various intervals of time maintaining the flow rate at 1.5 sccm at 25 °C. Next, we performed cyclic voltammetry (CV) experiments with the reaction mixture using 0.1 (M) KCl as an electrolyte in a potential range of +2 V to −2 V with respect to Ag/AgCl reference electrode in a standard three-electrode system. The reference electrode was filled with 0.1 (M) KCl solution. During the reaction, oxygen also evolved from the reaction mixture, which was confirmed and quantified from gas chromatography-mass spectrometry (GC-MS) technique and Clarke electrode.

All reaction samples were monitored by HITACHI—HPLC system equipped with binary 2130 pumps, a manual sampler, and 2490 refractive index detector, maintained at 50 °C. The products were separated in sugar ion-exclusion column, (250 × 4.8 mm) maintained at 60 °C using water as mobile phase with 0.8 mL min^{-1} flow rate. The HPLC system was controlled and processed by Inkarp software. Standard formic acid and formaldehyde solutions were prepared in milli-Q water before analysis to prevent the overloading of the column. All the experiments were conducted in triplicates and the average values were reported within the standard deviations of < 2.0%. Afterwards, 20 μL reaction mixture was taken out and further diluted with 10 mL double-distilled water. The high-performance liquid chromatography (HPLC) measurement was performed by injecting the above diluted reaction mixture in carbohydrate column with an external standard, i.e., 0.1 (M) formic acid solution. By using this technique, we confirmed the presence of formic acid in our reaction mixture. The quantitative measurement of formic acid was performed by the HPLC experiment.

The products were identified and analysed using a Trace 1300 GC and ISQ QD single quadruple GC-MS instrument with a TG-5MS capillary column (30 m × 0.32 mm × 0.25 μm) supplied by Thermo Fisher Scientific, India. The gas samples were detected using CarboPLOT 007 (25 m × 0.53 mm × 0.25 μm) in TCD detector.

To detect the oxygen evolved from the reaction, we first calibrated the YSI dissolved oxygen meter with degassed water. For this purpose, we first bubbled N_2 gas into the water for 2 h and then put YSI dissolve oxygen meter into this water and recorded the amount of oxygen present in it. Next, we took our reaction system that is, photo-illuminated sample and put dissolved oxygen meter into our reaction system and recorded the amount of oxygen present in the reaction system. From the difference of oxygen reading in YSI dissolved oxygen meter, we have calculated the oxygen formed in the reaction.

Supporting Information: PXRD patterns, FE-SEM images, HR-TEM images, EDX spectrum, FTIR spectra, Raman spectrum, TG traces,

chemical stability, N_2 sorption isotherms, CO_2 isotherm, photocatalytic studies, EPR, XPS, synthesis of ligand, Mass spectrum, NMR spectrum.

Acknowledgements

The authors acknowledge University Grant Commission (UGC) for fellowship, the Science and Engineering Research Board (SERB), New Delhi (PDF/2017/000676, grant no. EEQ/2016/000012), Fast Track, IISER Kolkata PRIS and FIRE grants, for financial support.

Conflict of interest

The authors declare no conflict of interest.

Keywords: catalysis · CO_2 reduction · formic acid · metal-organic framework · photochemistry

[1] O. K. Varghese, M. Paulose, T. J. LaTempa, C. A. Grimes, *Nano Lett.* **2009**, *9*, 731 – 737.
[2] Y. Liu, B. Huang, Y. Dai, X. Zhang, X. Qin, M. Jiang, M.-H. Whangbo, *Catal. Commun.* **2009**, *11*, 210 – 213.
[3] H. Cheng, B. Huang, Y. Liu, Z. Wang, X. Qin, X. Zhang, Y. Dai, *Chem. Commun.* **2012**, *48*, 9729 – 9731.
[4] S. C. Yan, S. X. Ouyang, J. Gao, M. Yang, J. Y. Feng, X. X. Fan, L. J. Wan, Z. S. Li, J. H. Ye, Y. Zhou, *Angew. Chem. Int. Ed.* **2010**, *49*, 6400 – 6404; *Angew. Chem.* **2010**, *122*, 6544 – 6548.
[5] Q. Liu, Y. Zhou, Z. Tian, X. Chen, J. Gao, Z. Zou, *J. Mater. Chem.* **2012**, *22*, 2033 – 2038.
[6] Q. Liu, Y. Zhou, J. Kou, X. Chen, Z. Tian, J. Gao, S. Yan, Z. Zou, *J. Am. Chem. Soc.* **2010**, *132*, 14385 – 14387.
[7] W. Lin, H. Frei, *J. Am. Chem. Soc.* **2005**, *127*, 1610 – 1611.
[8] H. Jiang, K.-i. Katsumata, J. Hong, A. Yamaguchi, K. Nakata, C. Terashima, N. Matsushita, M. Miyauchi, A. Fujishima, *Appl. Catal. B* **2018**, *224*, 783 – 790.
[9] S. Das, S. Biswas, T. Balaraju, S. Barman, R. Pochamoni, S. Roy, *J. Mater. Chem. A* **2016**, *4*, 8875 – 8887.
[10] S. Das, S. Kumar, S. Garai, R. Pochamoni, S. Paul, S. Roy, *ACS Appl. Mater. Interfaces* **2017**, *9*, 35086 – 35094.
[11] T. Kajiwara, M. Fujii, M. Tsujimoto, K. Kobayashi, M. Higuchi, K. Tanaka, S. Kitagawa, *Angew. Chem. Int. Ed.* **2016**, *55*, 2697 – 2700; *Angew. Chem.* **2016**, *128*, 2747 – 2750.
[12] J.-R. Li, J. Sculley, H.-C. Zhou, *Chem. Rev.* **2012**, *112*, 869 – 932.
[13] J.-R. Li, H.-C. Zhou, *Nat. Chem.* **2010**, *2*, 893 – 898.
[14] R. J. Kuppler, D. J. Timmons, Q.-R. Fang, J.-R. Li, T. A. Makal, M. D. Young, D. Yuan, D. Zhao, W. Zhuang, H.-C. Zhou, *Coord. Chem. Rev.* **2009**, *253*, 3042 – 3066.
[15] N. L. Rosi, J. Eckert, M. Eddaoudi, D. T. Vodak, J. Kim, M. O'Keeffe, O. M. Yaghi, *Science* **2003**, *300*, 1127 – 1129.
[16] J.-R. Li, J. Yu, W. Lu, L.-B. Sun, J. Sculley, P. B. Balbuena, H.-C. Zhou, *Nat. Commun.* **2013**, *4*, 1538.
[17] A. R. Millward, O. M. Yaghi, *J. Am. Chem. Soc.* **2005**, *127*, 17998 – 17999.
[18] J. M. Simmons, H. Wu, W. Zhou, T. Yildirim, *Energy Environ. Sci.* **2011**, *4*, 2177 – 2185.
[19] R. Tang, S. Zhou, Z. Yuan, L. Yin, *Adv. Funct. Mater.* **2017**, *27*, 1701102.
[20] J. Jiang, L. Huang, X. Liu, L. Ai, *ACS Appl. Mater. Interfaces* **2017**, *9*, 7193 – 7201.
[21] Y.-N. Gong, T. Ouyang, C.-T. He, T.-B. Lu, *Chem. Sci.* **2016**, *7*, 1070 – 1075.
[22] D. Wang, R. Huang, W. Liu, D. Sun, Z. Li, *ACS Catal.* **2014**, *4*, 4254 – 4260.
[23] J. Schneider, H. Jia, J. T. Muckerman, E. Fujita, *Chem. Soc. Rev.* **2012**, *41*, 2036 – 2051.
[24] M. B. Chambers, X. Wang, N. Elgrishi, C. H. Hendon, A. Walsh, J. Bonnefoy, J. Canivet, E. A. Quadrelli, D. Farrusseng, C. Mellot-Draznieks, *ChemSusChem* **2015**, *8*, 603 – 608.
[25] S. Wang, W. Yao, J. Lin, Z. Ding, X. Wang, *Angew. Chem. Int. Ed.* **2014**, *53*, 1034 – 1038; *Angew. Chem.* **2014**, *126*, 1052 – 1056.
[26] H.-Q. Xu, J. Hu, D. Wang, Z. Li, Q. Zhang, Y. Luo, S.-H. Yu, H.-L. Jiang, *J. Am. Chem. Soc.* **2015**, *137*, 13440 – 13443.
[27] H. Fei, M. D. Sampson, Y. Lee, C. P. Kubiak, S. M. Cohen, *Inorg. Chem.* **2015**, *54*, 6821 – 6828.
[28] Y. Lee, S. Kim, H. Fei, J. K. Kang, S. M. Cohen, *Chem. Commun.* **2015**, *51*, 16549 – 16552.
[29] K. M. Choi, D. Kim, B. Rungtaweevoranit, C. A. Trickett, J. T. D. Barmanbek, A. S. Alshammari, P. Yang, O. M. Yaghi, *J. Am. Chem. Soc.* **2017**, *139*, 356 – 362.
[30] S. Wang, X. Wang, *Appl. Catal. B* **2015**, *162*, 494 – 500.
[31] H. Zhang, J. Wei, J. Dong, G. Liu, L. Shi, P. An, G. Zhao, J. Kong, X. Wang, X. Meng, *Angew. Chem. Int. Ed.* **2016**, *55*, 14310 – 14314; *Angew. Chem.* **2016**, *128*, 14522 – 14526.
[32] M. Wang, J. Liu, C. Guo, X. Gao, C. Gong, Y. Wang, B. Liu, X. Li, G. G. Gurzadyan, L. Sun, *J. Mater. Chem. A* **2018**, *6*, 4768 – 4775.
[33] L. Ye, Y. Gao, S. Cao, H. Chen, Y. Yao, J. Hou, L. Sun, *Appl. Catal. B* **2018**, *227*, 54 – 60.
[34] Z.-C. Kong, J.-F. Liao, Y.-J. Dong, Y.-F. Xu, H.-Y. Chen, D.-B. Kuang, C.-Y. Su, *ACS Energy Lett.* **2018**, *3*, 2656 – 2662.
[35] C. Wang, Z. Xie, K. E. deKrafft, W. Lin, *J. Am. Chem. Soc.* **2011**, *133*, 13445 – 13454.
[36] S. Wang, J. Lin, X. Wang, *Phys. Chem. Chem. Phys.* **2014**, *16*, 14656 – 14660.
[37] Y. Fu, D. Sun, Y. Chen, R. Huang, Z. Ding, X. Fu, Z. Li, *Angew. Chem. Int. Ed.* **2012**, *51*, 3364 – 3367; *Angew. Chem.* **2012**, *124*, 3420 – 3423.
[38] D. Sun, W. Liu, M. Qiu, Y. Zhang, Z. Li, *Chem. Commun.* **2015**, *51*, 2056 – 2059.
[39] D. Sun, Y. Fu, W. Liu, L. Ye, D. Wang, L. Yang, X. Fu, Z. Li, *Chem. Eur. J.* **2013**, *19*, 14279 – 14285.
[40] D. Chen, H. Xing, C. Wang, Z. Su, *J. Mater. Chem. A* **2016**, *4*, 2657 – 2662.
[41] Y. Horiuchi, T. Toyao, K. Miyahara, L. Zakary, D. Do Van, Y. Kamata, T.-H. Kim, S. W. Lee, M. Matsuoka, *Chem. Commun.* **2016**, *52*, 5190 – 5193.
[42] G. G. Paille, M. Gomez-Mingot, C. Roch-Marchal, B. Lassalle-Kaiser, P. Mialane, M. Fontecave, C. Mellot-Draznieks, A. Dolbecq, *J. Am. Chem. Soc.* **2018**, *140*, 3613 – 3618.
[43] W. Lin, H. Frei, *J. Phys. Chem. B* **2005**, *109*, 4929 – 4935.
[44] M. L. Macnaughtan, H. S. Soo, H. Frei, *J. Phys. Chem. C* **2014**, *118*, 7874 – 7885.
[45] A. Schaate, P. Roy, T. Preuße, S. J. Lohmeier, A. Godt, P. Behrens, *Chem. Eur. J.* **2011**, *17*, 9320 – 9325.
[46] A. Das, S. Biswas, *Sens. Actuators B* **2017**, *250*, 121 – 131.
[47] R. Dalapati, S. Biswas, *Sens. Actuators B* **2017**, *239*, 759 – 767.
[48] G. C. Shearer, S. Chavan, S. Bordiga, S. Svelle, U. Olsbye, K. P. Lillerud, *Chem. Mater.* **2016**, *28*, 3749 – 3761.
[49] Z.-R. Jiang, H. Wang, Y. Hu, J. Lu, H.-L. Jiang, *ChemSusChem* **2015**, *8*, 878 – 885.
[50] Z. Zhang, J. Long, L. Yang, W. Chen, W. Dai, X. Fu, X. Wang, *Chem. Sci.* **2011**, *2*, 1826 – 1830.
[51] K. Maeda, K. Sekizawa, O. Ishitani, *Chem. Commun.* **2013**, *49*, 10127 – 10129.
[52] M. Sun, S. Yan, Y. Sun, X. Yang, Z. Guo, J. Du, D. Chen, P. Chen, H. Xing, *Dalton Trans.* **2018**, *47*, 909 – 915.
[53] J. Huang, X. Zhou, A. Lamprou, F. Maya, F. Svec, S. R. Turner, *Chem. Mater.* **2015**, *27*, 7388 – 7394.
[54] Z.-Q. Yu, X.-M. Xu, C.-Y. Hong, D.-C. Wu, Y.-Z. You, *Macromolecules* **2014**, *47*, 4136 – 4143.
[55] A. Coelho in *Topas Academics 4.2*, *Vol.* Coelho Software, Brisbane, **2007**.
[56] W. Kraus, G. Nolze in *PowderCell 2.4*, *Vol.* Berlin, **2000**.
[57] *Materials Studio Version 5.0*, *Vol.* Accelrys Inc., San Diego, **2009**.